RESEARCH ARTICLE
SPACE PHYSICS: IONOSPHERIC PHYSICS

Earth and Planetary Physics
9: 127–136, 2025
doi: 10.26464/epp2024075

3D tomographic analysis of equatorial plasma bubble using GNSS-TEC data from Indonesian GNSS Network

Ihsan Naufal Muafiry[1,4*], Prayitno Abadi[1,5], Teguh N. Pratama[1], Dyah R. Martiningrum[1,3], Sri Ekawati[1], Yuandhika G. Wismaya[2], Febrylian F. Chabibi[2], and Gatot H. Pramono[2]

[1]Research Center for Climate and Atmosphere, Indonesian National Research and Innovation Agency (BRIN), Bandung, Indonesia;

[2]Indonesian Geospatial Information Agency (BIG), Jakarta, Indonesia;

[3]Dept. of Physics, Faculty of Science, Universiti Teknologi Malaysia, Johor Bahru, Malaysia;

[4]Dept. Earth Planet Sci., Hokkaido University, Sapporo, Japan;

[5]School of Electrical Engineering, Telkom University, Bandung, Indonesia

Key Points:

- We present 3D tomography of Equatorial Plasma Bubble (EPB) following a geomagnetic storm on December 3, 2023, using GNSS-TEC data in Indonesia.
- A consistent 2D spatial distribution of the rate of TEC index (ROTI) and TEC depletion is first observed over time.
- The tomography results were validated through resolution tests and comparisons with Global Ionospheric Map (GIM) and International Reference Ionosphere (IRI), which show the capability of the Indonesian GNSS network for detailed EPB studies.

Citation: Muafiry, I. N., Abadi, P., Pratama, T. N., Martiningrum, D. R., Ekawati, S., Wismaya, Y. G., Chabibi, F. F., and Pramono, G. H. (2025). 3D tomographic analysis of equatorial plasma bubble using GNSS-TEC data from Indonesian GNSS Network. *Earth Planet. Phys.*, *9*(1), 127–136. http://doi.org/10.26464/epp2024075

Abstract: Equatorial Plasma Bubbles (EPBs) are ionospheric irregularities that take place near the magnetic equator. EPBs most commonly occur after sunset during the equinox months, although they can also be observed during other seasons. The phenomenon significantly disrupts radio wave signals essential to communication and navigation systems. The national network of Global Navigation Satellite System (GNSS) receivers in Indonesia (>30° longitudinal range) provides an opportunity for detailed EPB studies. To explore this, we conducted preliminary 3D tomography of total electron content (TEC) data captured by GNSS receivers following a geomagnetic storm on December 3, 2023, when at least four EPB clusters occurred in the Southeast Asian sector. TEC and extracted TEC depletion with a 120-minute running average were then used as inputs for a 3D tomography program. Their 2D spatial distribution consistently captured the four EPB clusters over time. These tomography results were validated through a classical checkerboard test and comparisons with other ionospheric data sources, such as the Global Ionospheric Map (GIM) and International Reference Ionosphere (IRI) profile. Validation of the results demonstrates the capability of the Indonesian GNSS network to measure peak ionospheric density. These findings highlight the potential for future three-dimensional research of plasma bubbles in low-latitude regions using existing GNSS networks, with extensive longitudinal coverage.

Keywords: EPB; Indonesian GNSS Network; 3D tomography

---

1. Introduction

Equatorial plasma bubbles (EPBs) are significant depletions in plasma density within the equatorial ionosphere. They vary in size from 50 to 1000 km, extending from the bottom side F region to altitudes of about 1000 km (Ossakow et al., 1979). These phenomena typically emerge after sunset, rising in altitude and stretching along geomagnetic field lines to the north and south, typically within a narrow band of ±20° dip latitude (Tsunoda, 1980; Tsunoda et al., 1982). Their zonal migration could reach up to 25° of the eastward direction or beyond (Abadi et al., 2024). Large-scale EPBs affect precise GNSS navigation (Yang Z et al., 2020) through rapid fluctuations in the amplitude and phase of radio signals (Kintner et al., 2007). The pre-reversal enhancement (PRE) of the eastward electric field induces upward plasma drifts at the equator after sunset (Farley et al., 1986). This upward plasma drift maintains the F layer at higher altitudes, which in turn increases the growth rate of Rayleigh–Taylor instability (RTI), leading to the generation of plasma bubbles (Kelley, 2009; Retterer and Roddy, 2014). Numerous studies on the spatial and temporal evolution of EPBs have been reported using various techniques, such as ionosonde observations (Abadi et al., 2023), Equatorial Atmospheric Radar (EAR) (Abadi et al., 2024), radio scintillation measurements (Abadi et al., 2024), all-sky optical instruments (Dos Santos Prol et al.,

---

Correspondence to: I. N. Muafiry, ihsa006@brin.go.id
Received 12 AUG 2024; Accepted 31 OCT 2024.

2018), Global Navigation Satellite Systems Radio Occultation (GNSS-RO) (Rajesh et al., 2022; Shinbori et al. 2023), and Global Navigation Satellite Systems Total Electron Content (GNSS-TEC) records (Pradipta et al., 2015; Husin et al., 2024).

Despite the development of numerous techniques, a significant challenge in characterizing plasma bubbles persists, because sensor instruments are limited in their ability to monitor plasma depletions over large areas (Dos Santos Prol et al., 2018). With the extensive installation of ground-based GNSS receivers worldwide, initially for studies of crustal movement and land mapping activities, the observation of plasma bubbles over large areas has become more feasible using GNSS-TEC parameters from these GNSS stations. For example, Carmo et al. (2022) reported unusual pre-sunrise plasma bubbles using a dense GNSS network in South America. Cherniak and Zakharenkova (2018) utilized GNSS networks across ~50 European countries to study ionospheric disturbances caused by a geomagnetic storm in 2015. The latest extensive studies of equatorial plasma bubbles using the dense-large coverage GNSS nation network in Indonesia are reported in Abadi et al. (2025).

Indeed, while GNSS-TEC parameters cannot fully replace the advantages of other ionosphere sensors (e.g. monitoring high spatial resolution of vertical plasma variability, as ionosonde measurements can), they provide an alternative solution for ionospheric studies, both horizontally due to significant GNSS station distribution (Sori et al., 2021; Heki, 2021), and vertically by performing 3D tomography with GNSS lines-of-sight (Muafiry et al., 2018; Song R et al., 2022).

The primary objective of this study is to examine EPBs in greater detail using 3D tomography analysis from GNSS-TEC data in Southeast Asian sector, particularly over Indonesian Region. Previously, 3D tomography study of EPBs using GNSS-TEC parameters has been reported for Brazilian (Dos Santos Prol et al., 2018) and Southeast Asian limited to Malaysian Peninsular (Khamdan et al., 2021) regions. For the latter, due to narrow zonal distance of the ground GNSS stations used, only two out of the three clusters of EPBs can be detected. The Indonesian GNSS Continuously Operating Reference System (Ina-CORS), consisting of more than 300 stations with ~20–30 km average of horizontal distances ranging from 90°E to 140°E (>30° longitudinal range), offers a comprehensive dataset in analyzing EPB and other ionospheric irregularities using the GNSS-TEC parameters. Considering the EPB characteristics (i.e. size, latitudinal extension and longitudinal migration) from previous studies, Ina-CORS configurations are highly sufficient to capture the zonal and meridional evolutions of EPBs in Southeast Asian sector. Abadi et al. (2025) introduced a 2-dimensional map of GNSS rate of TEC index (ROTI) from the Indonesian network, and found the datasets useful for monitoring the complete evolution of plasma bubbles in this sector, from generation to dissipation. (Interested readers may use the ROTI map of 10-minute intervals from the Indonesian network, for records running from August 2023 until present, at the website: https://gatotkaca.brin.go.id/petaionosfer/. There is a delay of at least one month for data availability.)

In this study, we preliminarily utilized 30-second interval Ina-CORS data to gain a more thorough understanding of the behavior of ionospheric plasma that contributes to the formation of plasma bubble in three dimensions. We examined both the 2D and 3D structures and the developments of EPBs on December 3rd, 2023, which corresponds to day of year (DOY) 337, two days after a geomagnetic storm (Sun WJ et al., 2024). In addition to the ROTI map, the extracted TEC depletion associated with plasma bubbles was used for 2D analysis. The consistency in generation and evolution from these two methods was initially confirmed to assess the accuracy of the isolation method, and we reported this result in Section 2. Furthermore, we used isolated TEC as input to our 3D tomography programs to visualize the three-dimensional structures and evolution of plasma bubbles. The robustness of our tomography results was examined through at least three different procedures: (1) resolution test of tomography voxels; (2) comparison of observed vertical TEC (VTEC) from tomography results with the 30-minute VTEC provided by the Global Ionospheric Map (GIM); and (3) comparison of the three-dimensional vertical profile with International Reference Ionosphere (IRI) vertical profile. The first testing procedure is detailed in Section 2, while the second and third procedures are reported in Section 3 of this paper. In the last part of Section 3, we discuss the possible mechanism of EPBs generation on DOY 337, 2023, based on both the 2D and 3D analyses we performed. Concluding thoughts and future outlooks are presented in Section 4.

2. Data and Method

2.1 Indonesian GNSS Network and GNSS-TEC Measurement

Here, we utilized 30-second GNSS-TEC data derived from raw Receiver Independent Exchange Format (RINEX) data, from approximately 300 GNSS stations in Indonesia managed by the Indonesian Geospatial Agency (BIG). We used data from all available GPS satellites, with a condition of elevation angles higher than or equal to 30º. In Figure 1a, black squares show the stations used in this study, for which the zonal extension of the network is more than 30º. The VTEC is first calculated for each GPS station–satellite pair by removing the inter-frequency biases from both receiver and satellite. Total biases are obtained from the minimum differences of observed VTEC from the GIM (Global Ionospheric Map), with VTEC calculated as the multiplication product of slant TEC (STEC) with cosine of the incidence angles at a height of 300 km. We followed the STEC calculation performed by Heki (2006). Figure 1b is the VTEC time series observed by CPSM station (indicated by the larger black square in Figure 1a). The diurnal variation of VTEC can clearly be seen. For example, VTEC is higher during local noon and lower after sunset (Figure 1b). In this study, to better analyze the temporal and spatial variations of plasma bubble, we calculated VTEC for all BIG stations available.

2.2 Extraction of Ionospheric Plasma Bubble

To extract the TEC depletion relevant to plasma bubbles, we subtracted the VTEC with a running average for each line-of-sight (LoS), following Fig. S8 in Pradipta et al. (2015), but with longer period (e.g. 120 minutes moving averages). This anticipated the

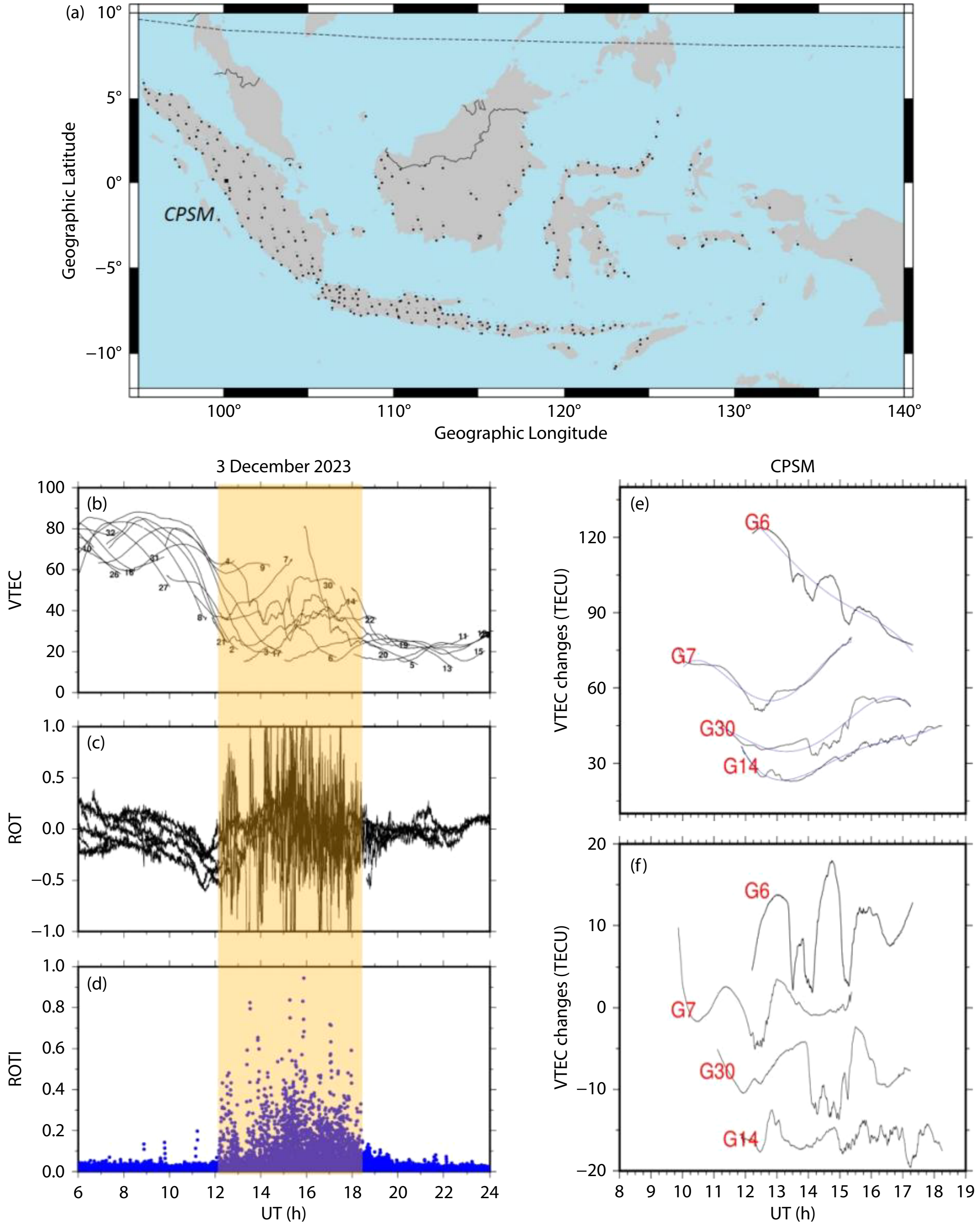

Figure 1. (a) Map of GNSS stations in Indonesia (black squares), managed by the Indonesian Geospatial Information Agency (BIG). CPSM = CORS at Pasaman, Sumatra. (b) VTEC measured from CPSM station on December 3rd, 2023. (c) Rate of TEC changes. (d) Rate of TEC index calculated from all available GPS satellites in blue dots pairing with CPSM. (e) Application of 120 minutes moving average in blue curves to VTEC data in black curves from G6, G7, G30, and G14 (G stands for satellite GPS). VTEC in (e) is same as the curves given in (b). (f) Extracted VTEC; e.g. subtraction product between VTEC and moving average curve. Brown shadow in (b–d) panels highlights EPB onset time recorded by CPSM station. The black dashed curve in (a) is an approximated position of Earth's magnetic equator.

disappearance of expected TEC depletion. The relative change in VTEC can be seen in Figure 1f, and samples of TEC extraction using moving average are presented in Figure 1e. From these two figures, G6 and G30 shows TEC depletion of more than 10 TECU (1 TECU equals to 10^{16} el/m^2). We then plotted EPB extraction results onto a 2D map for individual LoSs intersecting at a height of 300 km (e.g. sub-ionospheric piercing point), with a condition of relative change in VTEC below −5 TECU (Figures 2d and 2e). The LoSs with VTEC anomalies greater than −5 TECU were converted to zero for visualization purposes. This also highlights the limitations of the running mean method in isolating TEC depletion (for example, the extraction results still contain positive changes). In

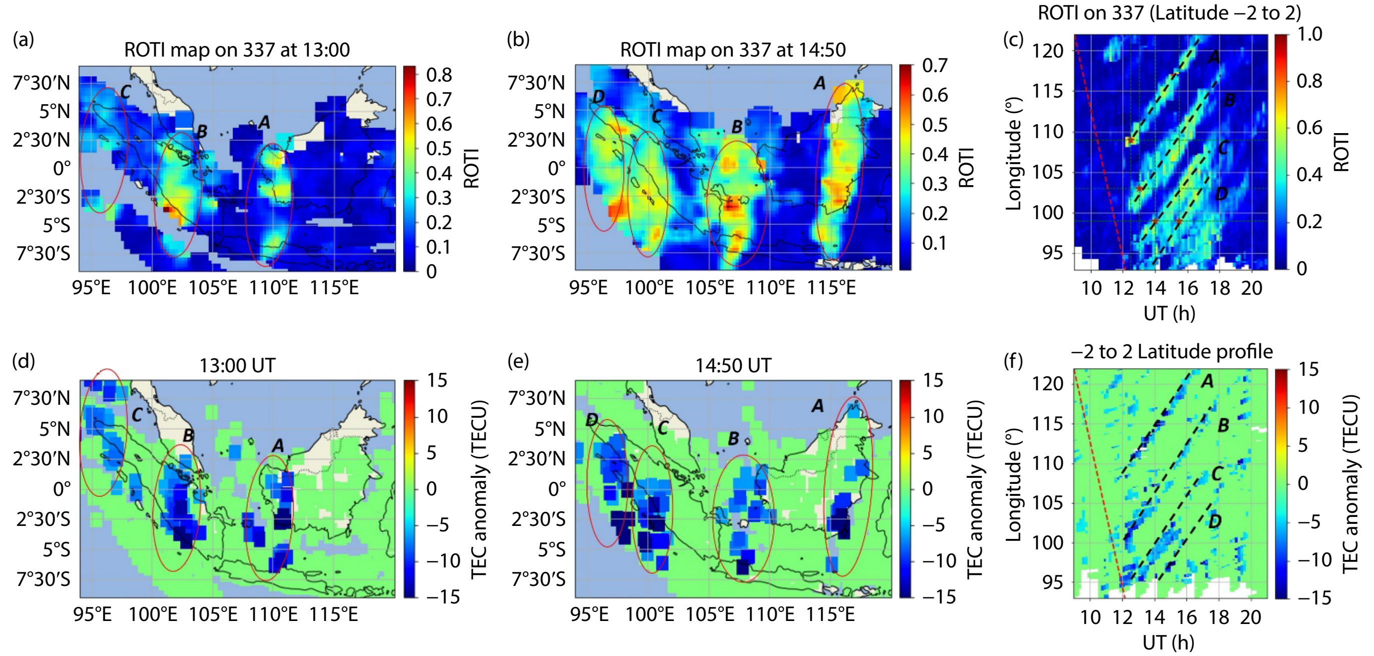

Figure 2. The sub-ionospheric piercing point (SIP) distribution at 350 km altitude with ROTI at 13:00 UT (a) and 14:50 UT (b). (c) Time-latitudinal profile of ROTI map detecting at least four cluster of EPB after sunset (EPBs A–D). Red dashed line in (c) shows sunset terminator. (d) and (e) show SIP at 300 km height with extracted VTEC of less than −5 TECU (TEC anomaly) at 13:00 UT and 14:50 UT, respectively. (f) is similar to (c), but for anomalous TEC.

contrast, the detrending method proposed by Pradipta et al. (2015) is able to recognize the presence of TEC depletions even at low intensities, without any positive changes. Above all, with this simpler method, at least four clusters of TEC depletion associated with EPBs were identified at 13:00 UT, and all of them were migrating eastward as shown in Figure 2e (SIP distribution at 14:50 UT).

In this study, we also confirmed the generation of such EPBs using ROTI calculated from the same stations. Figures 1c and 1d show the rate of TEC changes and the corresponding index, which ranges from 0 to 1. The index begins to increase when TEC depletion starts. The TEC depletion associated with EPBs recorded by the CPSM station occurred from 12:00 to 18:00 UT (Figures 1b–1d). However, analyzing EPBs from only one station may be insufficient; thus, a ROTI map was created using data from all available stations (Figure 2a and 2b). Figure 2a and 2b are derived from numerical data of Indonesian ROTI map given in Abadi et al. (2025). Details of the ROTI map generation from the GNSS network in Indonesia can be found in Abadi et al. (2025). Figure 2c depicts zonal cross-section of ROTI variation (at ~0° N) from the map on December 3rd, 2023. This profile resembles the TEC depletion calculated by 120-minute running averages, capturing several clusters of EPBs migrating eastward after local sunset (Figure 2f). These 2D results show consistency of EPB generation both spatially and temporally.

2.3 3D Tomography of Ionospheric Plasma Bubble

Our goal is to capture EPB images with tomography, using relative changes of TEC by 120-minutes running average. In order to quantitatively assess the accuracy of the method, 3D tomography of ionospheric electron density is initially performed using VTEC measured from every single GPS satellite–receiver pair as input data. We expect that our 3D tomography image of background electron density can be well-evaluated by comparing the results with established independent references (e.g., International Reference Ionosphere Model and Global Ionospheric Map) on a daily basis. Our 3D tomography voxel size is 1.2°E-W, 2.3°N-S, and 120 km in height, covering the Indonesian region from 94.2° E to 121.8°E, 11.95°S to 8.95°N, and 120–840 km in altitude.

A tomography resolution test is initially performed using the classical checkerboard pattern, distributing alternating positive and negative electron density (±0.3 TECU) to the constructed voxels (Figure 3a). We then synthesized the electron density of the tests for each LoS using their real geometry positions. The ray path is assumed to be the sum product (in unit length) of electron density from the penetrated voxels. Also, in our current program, we used IRI profile at 1°S and 111°E (e.g. the location where EPB is expected) as an input for constraining the electron density peak altitude for all available voxels. The uniform STEC observation errors of 0.1 TECU are also assumed here. Details of the algorithm for the 3D tomography can be found in Muafiry and Heki (2020).

Figure 3b shows that the input patterns are reasonably recovered through the inversion algorithm, except in the south–west voxels, which show clear smearing covering the Indian Ocean region, indicating low accuracy of the spatial structure on these voxels. We also confirmed that the checkerboard test at all other epochs (with 2-minute intervals) used in this study has the same accuracy as those performed at 14:50 UT. The main interest of 3D tomography studies is to better understand the vertical variability of ionospheric irregularities. We found that, unfortunately, after some modifications to the voxel size, the 120 km altitude resolution

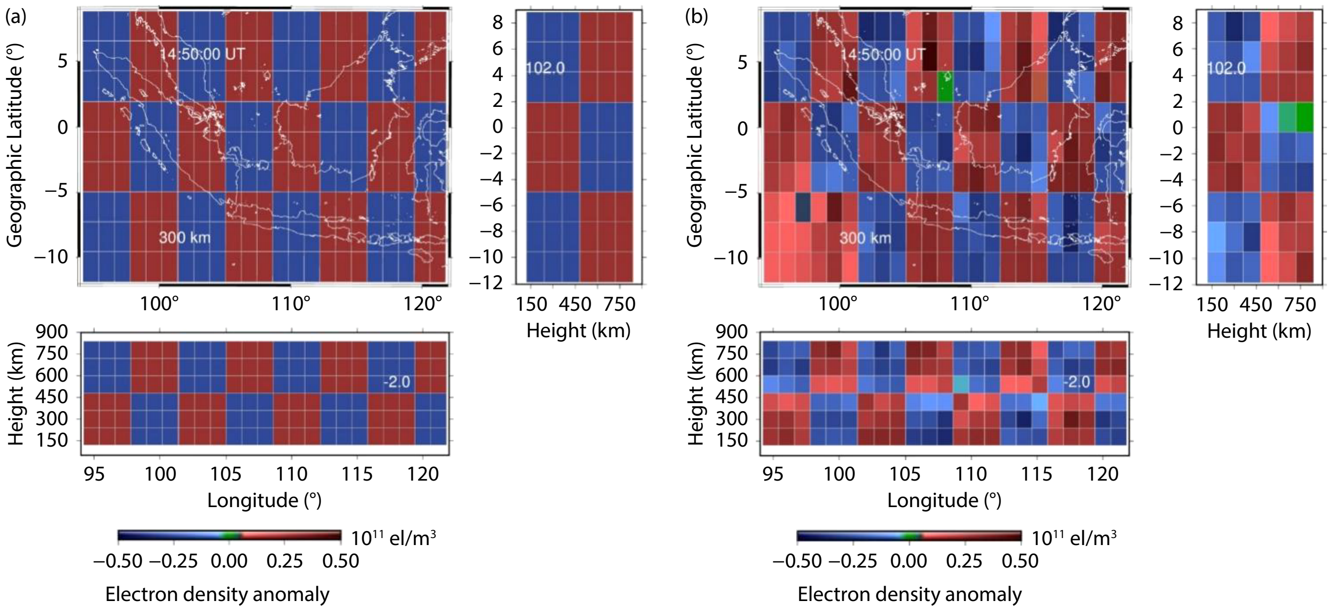

Figure 3. Resolution test of the tomography voxels using classical checkerboard pattern with alternated ± 0.3 TECU at 14:50 UT (a). The inverted model (b) shows results of the test in 300 km (upper left panel), 102° E (right panel), and 2° S (bottom panel).

appears to be the best option with the current algorithm and datasets. One might expect a vertical resolution of at least 30 km, but we found smearing in almost all boxes at this resolution. Nevertheless, after obtaining good results from the tomography resolution test in Figure 3, we were confident enough to continue the tomography studies using real observation data over the Indonesian region.

3. Results

3.1 3D Tomography of VTEC

Figures 4a and 4b display the 3D tomography results of electron

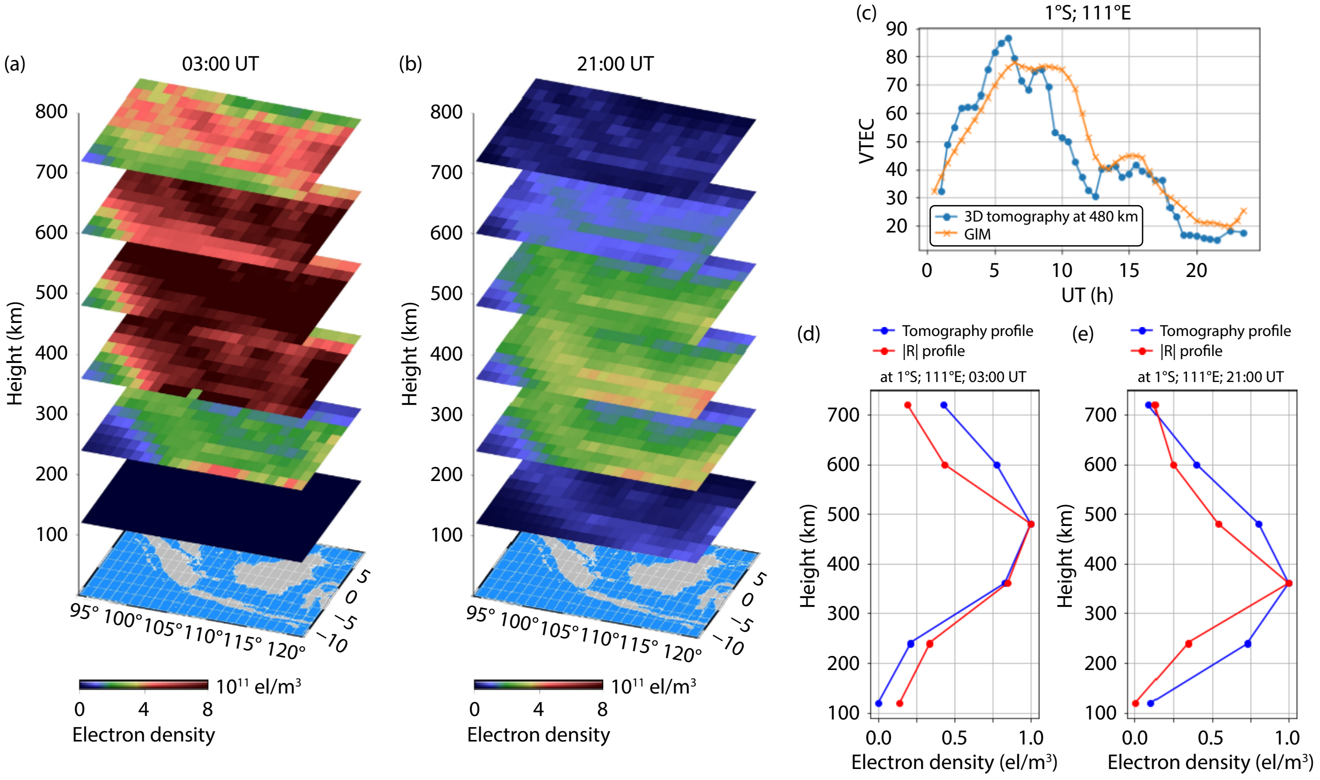

Figure 4. Tomography result with VTEC as input data at 03:00 UT (a) and 21:00 UT (b). Comparison of one day (December 3rd, 2024 at 1°S and 111°E) VTEC from tomography result in blue curve and Global Ionospheric Map in orange curve (c). Vertical profile of 3D tomography in blue curve and International Reference Ionosphere (IRI) in red curve at 03:00 UT (d) and at 21:00 UT (e) at 1°S and 111°E.

density at 03:00 UT (before EPB occurs) and 21:00 UT (midnight time without EPB) on December 3, 2023, using VTEC data as an input. Although the resolution is coarse and the voxel size is large, the tomogram shows maximum electron density to be located in F region (around 360–480 km altitude) for both epochs. For further evaluation of the tomogram, we compared the daily variation of VTEC from GIM, NASA CDDIS (cddis.nasa.gov), at 1°S and 111°E (Figure 4c). There, the tomography electron density is normalized at 480 km. Although the results show variations with the VTEC from GIM, the overall daily trends from both datasets are very similar. Such variations may originate from dense GNSS receiver data used in the tomography method. Next, the vertical profile of electron density from tomography is also evaluated by IRI models (Bilitza et al., 2022), as shown in Figures 4d (at 03:00 UT) and 4e (at 21:00 UT).

We found that the results of the vertical tomographic profile show good alignment in the peak density region, but do not fit well with the IRI model on the top and bottom sides. This discrepancy may come from uniform altitudinal constraint in the tomography program (Muafiry and Heki, 2020). After some confirmations with the electron density profile of GNSS-RO during the same period, in our 3D tomography studied area we found differences in the peak altitudes of vertical profiles between lower and higher latitudes. In the future, the accuracy of the upper and lower profiles could be improved by incorporating multiple ionospheric observation techniques, such as GNSS-RO, Ionosonde, and Equatorial Atmospheric Radar. Nevertheless, the most important goal of this study is to achieve at least a best-fit in the peak density region, which helps to indicate the actual altitude of the EPBs where the electron density is at its maximum.

We next attempted to capture the EPBs using 3D tomography of VTEC by observing the latitudinal–height profile (Figure 5a) at 14:50 UT, when at least four clusters of EPB occurred, according to Figures 2b and 2e. As expected, the profile shows higher electron density in F layer. Interestingly, electron density depletion is identified along at least four different longitudes associated with EPBs detected in ROTI and TEC anomaly maps. Their longitudinal positions are approximately similar to 2D analysis results in Figures 2b and 2e.

3.2 3D Tomography of Equatorial Plasma Bubble

After having good spatial and temporal correlation of four EPBs cluster between the 2D map and 3D structures from VTEC input data, we now use relative changes of TEC (TEC depletion) extracted by 120-minutes running mean as an input to 3D tomography. Figure 5b presents the profile from extracted EPBs with a similar setting to Figure 5a. The location of extracted EPBs and background depletion are similar, although the latter shows larger coverage of EPBs. This might be due to instability of the TEC extraction method.

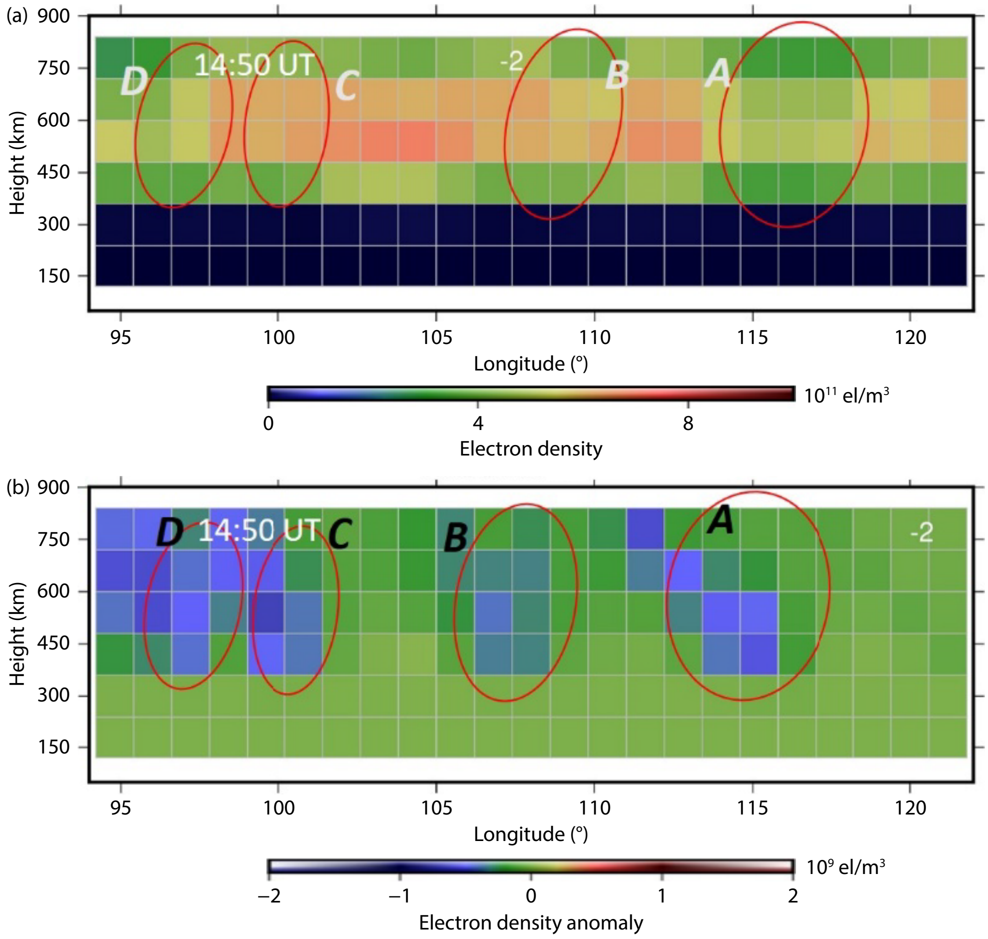

Figure 5. Altitudinal–latitudinal profile at 2°S from tomogram using VTEC (a) and extracted TEC (b) at 14:50 UT.

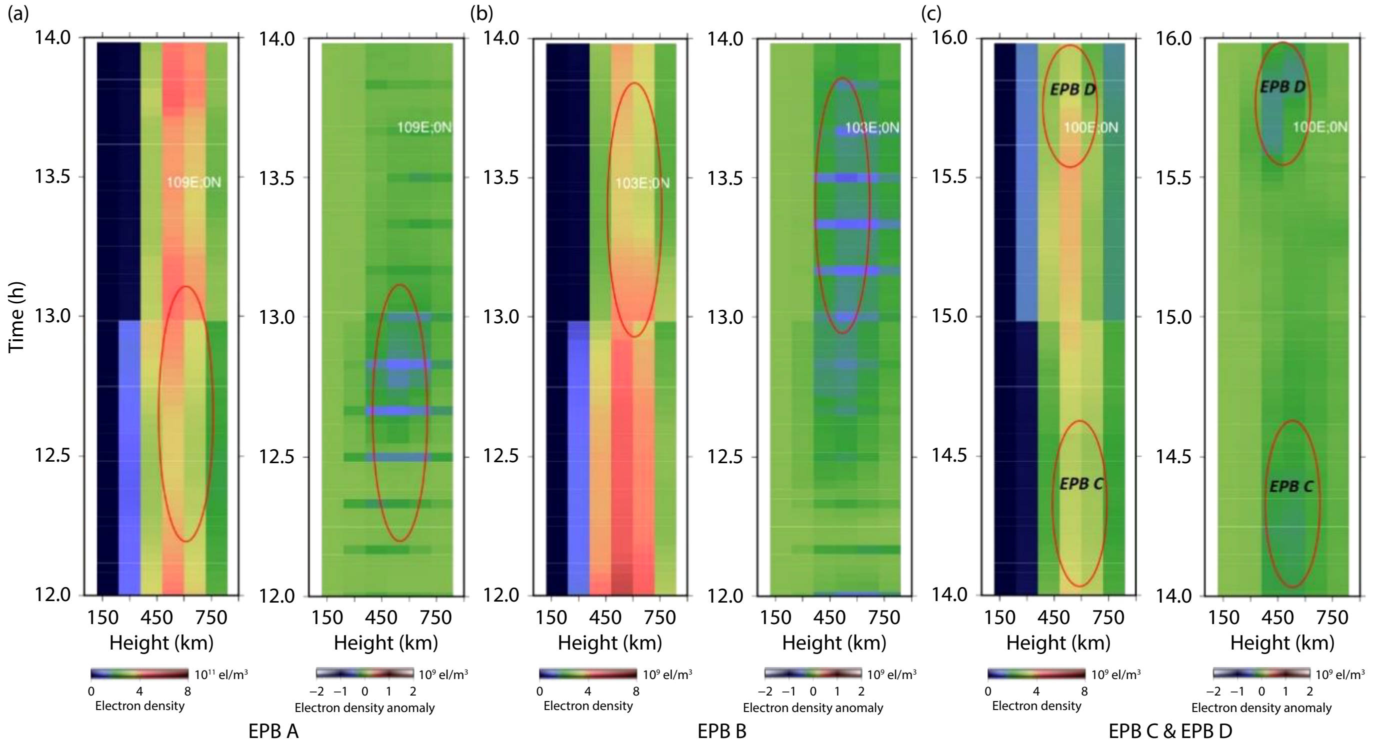

Figure 6. Time–height cross-section of electron density and electron density anomaly were taken from various locations and times, expressed as three red stars in Figure 2c. (a) Profile for detection of EPB A, as shown in Figure 2c from 12:00–14:00 UT. (b) and (c) are profiles for showing temporal evolution of EPBs B and C–D, respectively.

For detailed studies of EPBs, we plotted time–altitudinal profile derived from tomogram using VTEC and extracted TEC at two minutes interval. The results (Figures 6a–6c) show onset time of depleted electron background and extracted EPBs, according to time–latitudinal profile of the 2D ROTI map in Figure 2c. In this context, the longitudinal positions and times of four clusters of EPBs were detected (e.g. star symbols in Figure 2c) and used for further detailed studies. EPB A is approximately at 109°E at ~12:00 UT, EPB B is around 103°E at ~13:00 UT, and EPBs C and D are located around 100°E at ~14:00 UT and at ~15:00 UT, respectively.

Figures 6a–6c shows 3D structures of the EPB clusters from their appearance to dissipation at each selected location (marked by red circles). The structures are comparable between the electron background depletion and extracted EPB. For example, each EPB recorded in a relatively similar period across all EPB clusters. However, we realized there is a time lag between them, which we believe is due to the instability of the TEC change extraction method. Nevertheless, the reconstructed profile clearly depicts all EPB clusters stretching from lower to upper ionospheric F layers.

3.3 Process of Plasma Bubble Generation

We next presented the tomogram's height–latitude profile and found prominent feature of EPB clusters by measuring contrast with the background amplitudes in Figure 7b. Each expected plasma bubble (EPBs A–D) can be identified as an electron density depletion background, between two peaks on the eastern and western sides of the depletion structures. The high-dense electron background brought by possible eastward neutral wind significantly increases the rate of Rayleigh–Taylor instability (RTI), thereby triggering the formation of plasma bubbles (Farley et al., 1986).

Figure 7a illustrates the height-latitude profile from the tomogram at 12:20–13:00 UT, corresponding to the sunset period on DOY 337. During this period, we observed eastward electron movement indicated by two slopes in black solid lines. Extending the observation period, as shown in Figure 7b, reveals that this eastward background migration continues at least until 16:00 UT.

Because it is challenging to quantitatively discriminate the background movement in the tomogram, we extracted the electron background at 480 km, from the height–latitude profile at 12:00 until 16:00 UT (Figure 7c). The plot shows some peaks for every single epoch associated with high electron density and they are moving eastward. However, in order to calculate the speed of the movement, we focused on the first peak on the western side of the 12:00 UT profile, and traced the closest peak at the next epoch, as pointed out by blue arrows. Such processes were guided by tomograms from Figures 7a and 7b to accurately capture the evolution of the EPB. The average speed of the electron background's eastward migration from 12:00–16:00 UT is calculated to be 64.81 m/s.

Based on this observed eastward electron background speed, it is similar to the speed of the eastward neutral wind. Further, we also confirmed with in situ Gravity Recovery and Climate Experiment Follow-on (GRACE-FOs) the neutral wind speed observation at a similar time (around sunset) and location (around Indonesia) to be 35–150 m/s (Siemes et al., 2023). Previously, Abadi et al. (2021) also reported that the speed of the eastward neutral wind ranges

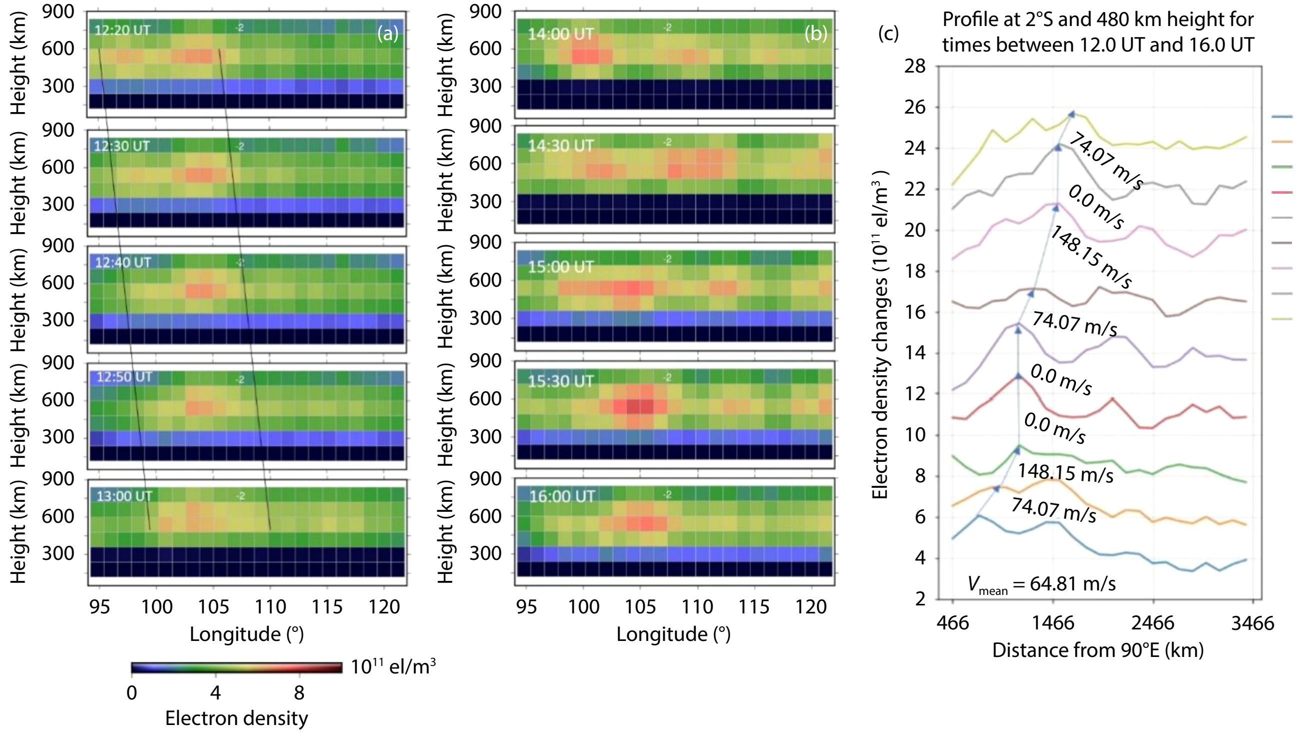

Figure 7. Eastward movement of electron background observed by tomogram at latitude 2°S from 12:20–13:00 UT (a). (b) is the same as (a), but from 14:00 to 16:00 UT, with a 30 minute interval. (c) is a profile of electron density background at 480 km altitude from 12:00–16:00 UT. The average eastward electron background velocity is calculated to be 64.81 m/s.

from approximately 75 m/s to 150 m/s. Here, we assume that this eastward movement of the high-density electron background is strongly influenced by the eastward neutral wind.

Previous studies have shown that the eastward neutral wind significantly contributes to the PRE by generating a downward polarization electric field in the F region (Rishbeth, 1971; Farley et al., 1986). Additionally, Abadi et al. (2021) suggests that the equatorial electrojet (EEJ) also contributes to PRE, by giving a positive correlation indicating that stronger EEJ enhances PRE strength. Despite both factors playing significant roles, the eastward neutral wind's impact appears more direct and fundamental, as it consistently drives the dynamo process, whereas EEJ's influence is supportive but less dominant (Otsuka et al., 2023).

4. Conclusions

In this study, we conducted preliminary 3D tomographic analysis of Equatorial Plasma Bubbles (EPBs) using GNSS-TEC data collected by Indonesia's extensive GNSS network on December 3, 2023 (DOY 337). The 2D snapshots from ROTI and extracted TEC confirm the presence of at least four EPBs occurring after sunset, as both displayed high index value and TEC depletions, respectively.

The Indonesian GNSS network reveals a tomogram in which the maximum electron density is primarily located in the F region, which aligns well with the IRI vertical profile. Although we found that the top and bottom sides of the tomography profile overestimate IRI, this result at least demonstrates the capability of the Indonesian GNSS network to capture the peak density region. An improved GNSS-based tomography (e.g. combining GNSS-TEC and GNSS-RO data) for ionospheric studies has been developed by Dos Santos Prol et al. (2018), and represents an area of future research for our team. Additionally, four clusters of EPBs were also identified in our tomogram from two different inputs to the 3D tomography program: VTEC and extracted TEC with a 120-minute running mean. These 3D structures agree with the 2D analyses of ROTI and TEC depletions spatially and temporally.

The 3D-constructed electron density depletion patterns associated with four EPB structures (on DOY 337) suggest a good spatial correlation with the dynamics of the surrounding electron density. Eastward electron density migration was detected after sunset in the tomogram, with an average speed of 64.81 m/s, indicating the speed of the eastward neutral wind. However, we noted some overestimation in the tomogram which may due to the instability of TEC extraction process. This might reduce the accuracy of identified EPBs, highlighting the need for further refinement of data processing techniques in the future.

Above all, this research underscores the potential of 3D tomography in a low-latitude region with a longitudinal extension greater that 30°, paving the way for future studies aimed at improving the accuracy of ionospheric analyses in equatorial regions.

Acknowledgements

The authors would like to acknowledge the Indonesian Geospatial Information Agency for providing GNSS observable data in RINEX files, which were crucial in generating GNSS-TEC parameters over the Indonesian region (https://srgi.big.go.id/). Global Ionospheric Map and International Reference of Ionosphere used in this study were downloaded from the internet (cddis.nasa.gov and https://kauai.ccmc.gsfc.nasa.gov/ respectively). INM expresses deep gratitude to the National Institute of Information and Communication Technology International Exchange Program 2024–2025 (No. 2024–007) for their invaluable support in this research. 3D tomography software is available at Prof. Kosuke Heki's (Hokkaido University, Japan) personal homepage (https://www.ep.sci.hokudai.ac.jp/~heki/software.htm). INM also extends thanks to him and Dr. Susumu Saito from the Electronic Navigation Research Institute for insightful face-to-face discussions. PA acknowledges the support from the 2024 Japan Student Services Organization Research Follow-up Fellowship for a 90-day research visit at the Institute for Space–Earth Environmental Research, Nagoya University, Japan. PA also acknowledges the support received from Telkom University under the "Skema Penelitian Terapan Periode I Tahun Anggaran 2024", and the Memorandum of Understanding for Research Collaboration on Regional Ionospheric Observation (No: 092/SAM3/TE-DEK/2021).

References

Abadi, P., Otsuka, Y., Liu, H. X., Hozumi, K., Martinigrum, D. R., Jamjareegulgarn, P., Thanh, L. T., and Otadoy, R. (2021). Roles of thermospheric neutral wind and equatorial electrojet in pre-reversal enhancement, deduced from observations in Southeast Asia. *Earth Planet. Phys.*, *5*(5), 387–396. https://doi.org/10.26464/epp2021049

Abadi, P., Ali Ahmad, U., Otsuka, Y., Jamjareegulgarn, P., Almahi, A., Perwitasari, S., Supriadi, S., Harjupa, W., and Septiawan, R. R. (2023). Assessing the potential of ionosonde for forecasting post-sunset equatorial spread F: An observational experiment in Southeast Asia. *Earth Planets Space*, *75*, 185. https://doi.org/10.1186/s40623-023-01941-1

Abadi, P., Otsuka, Y., Saito, S., Yamamoto, M., Perwitasari, S., Muafiry, I. N., Putra, A. Y., and Faturahman, A. (2024). Longitudinal range of the eastward-traveling equatorial plasma bubble inducing ionospheric scintillation. *Space Wea.*, *22*(8), e2024SW003908. https://doi.org/10.1029/2024SW003908

Abadi, P., Muafiry, I. N., Pratama, T. N., Putra, A. Y., Suraina, Pramono, G. H., Wibowo, S. T., Chabibi, F. F., Ahmad, U. A., … Asnawi.(2025). Leveraging ROTI map derived from Indonesian GNSS receiver network for advancing study of Equatorial Plasma Bubble inSoutheast/East Asia. *Earth Planet. Phys.*, *9*(1), 101–116. https://doi.org/10.26464/epp2025007

Bilitza, D., Pezzopane, M., Truhlik, V., Altadill, D., Reinisch, B. W., and Pignalberi, A. (2022). The International Reference Ionosphere model: A review and description of an ionospheric benchmark. *Rev. Geophys.*, *60*(4), e2022RG000792. https://doi.org/10.1029/2022RG000792

Carmo, C. S., Denardini, C. M., Figueiredo, C. A. O. B., Resende, L. C. A., Moro, J., Silva, R. P., Nogueira, P. A. B., Chen, S. S., Picanço, G. A. S., and Barbosa Neto, P. F. (2022). Findings of the unusual plasma bubble occurrences at dawn during the recovery phase of a moderate geomagnetic storm over the Brazilian sector. *J. Atmos. Sol.-Terr. Phys.*, *235*, 105908. https://doi.org/10.1016/j.jastp.2022.105908

Cherniak, I., and Zakharenkova, I. (2018). Large-scale traveling ionospheric disturbances origin and propagation: Case study of the December 2015 geomagnetic storm. *Space Wea.*, *16*(9), 1377–1395. https://doi.org/10.1029/2018SW001869

Dos Santos Prol, F., Hernández-Pajares, M., de Assis Honorato Muella, M. T., and De Oliveira Camargo, P. (2018). Tomographic imaging of ionospheric plasma bubbles based on GNSS and radio occultation measurements. *Remote Sens.*, *10*(10), 1529. https://doi.org/10.3390/rs10101529

Farley, D. T., Bonelli, E., Fejer, B. G., and Larsen, M. F. (1986). The prereversal enhancement of the zonal electric field in the equatorial ionosphere. *J. Geophys. Res.: Space Phys.*, *91*(A12), 13723–13728. https://doi.org/10.1029/JA091iA12p13723

Heki, K. (2006). Explosion energy of the 2004 eruption of the Asama Volcano, Central Japan, inferred from ionospheric disturbances. *Geophys. Res. Lett.*, *33*(14), L14303. https://doi.org/10.1029/2006GL026249

Heki, K. (2021). Ionospheric disturbances related to earthquakes. In C. S. Huang, et al. (Eds.), *Ionosphere Dynamics and Applications* (pp. 511–526). American Geophysical Union. https://doi.org/10.1002/9781119815617.ch21

Husin, A., Dear, V., Faturahman, A., Anggarani, S., Mardiani A. S., Purwono, A., Harjosuwito, J., and Pradipta, R. (2024). Simultaneous observation of equatorial plasma bubbles and traveling ionospheric disturbances over Indonesia following the 15 January 2022 Tonga volcano eruption. *Space Wea.* https://doi.org/10.22541/essoar.171828406.62804983/v1

Kelley, M. C. (2009). *The Earth's Ionosphere: Plasma Physics and Electrodynamics* (2nd ed). Amsterdam: Academic Press.

Khamdan, S. S., Musa, T. A., and Buhari, S. M. (2021). Detection of equatorial plasma bubbles using GPS ionospheric tomography over peninsular Malaysia. *J. Inf. Syst. Technol. Manage.*, *6*(24), 152–160. https://doi.org/10.35631/JISTM.624016

Kintner, P. M., Ledvina, B. M., and de Paula, E. R. (2007). GPS and ionospheric scintillations. *Space Wea.*, *5*(9), S09003. https://doi.org/10.1029/2006SW000260

Muafiry, I. N., Heki, K., and Maeda, J. (2018). 3D tomography of midlatitude sporadic-E in Japan from GNSS-TEC data. *Earth Planets Space*, *70*, 45. https://doi.org/10.1186/s40623-018-0815-7

Muafiry, I. N., and Heki, K. (2020). 3D tomography of the ionospheric anomalies immediately before and after the 2011 Tohoku-Oki (M_w9.0) earthquake. *J. Geophys. Res.: Space Phys.*, *125*(10), e2020JA027993. https://doi.org/10.1029/2020JA027993

Ossakow, S. L., Zalesak, S. T., McDonald, B. E., and Chaturvedi, P. K. (1979). Nonlinear equatorial spread *F*: Dependence on altitude of the *F* peak and bottomside background electron density gradient scale length. *J. Geophys. Res.: Space Phys.*, *84*(A1), 17–29. https://doi.org/10.1029/JA084iA01p00017

Otsuka, Y., Abadi, P., Hozumi, K., and Almahi, A. (2023). Equinoctial asymmetry of plasma bubble occurrence and electric field at evening: GPS and ionosonde measurements in Southeast Asia. *J. Atmos. Sol.-Terr. Phys.*, *252*, 106136. https://doi.org/10.1016/j.jastp.2023.106136

Pradipta, R., Valladares, C. E., and Doherty, P. H. (2015). An effective TEC data detrending method for the study of equatorial plasma bubbles and traveling ionospheric disturbances. *J. Geophys. Res.: Space Phys.*, *120*(12), 11048–11055. https://doi.org/10.1002/2015JA021723

Rajesh, P. K., Lin, C. C. H., Lin, J. T., Lin, C. Y., Liu, J. Y., Matsuo, T., Huang, C. Y., Chou, M. Y., Yue, J., … Tsai, H. F. (2022). Extreme poleward expanding super plasma bubbles over Asia-Pacific region triggered by Tonga volcano eruption during the recovery-phase of geomagnetic storm. *Geophys. Res. Lett.*, *49*(15), e2022GL099798. https://doi.org/10.1029/2022GL099798

Retterer, J. M., and Roddy, P. (2014). Faith in a seed: on the origins of equatorial plasma bubbles. *Ann. Geophys.*, *32*(5), 485–498. https://doi.org/10.5194/angeo-32-485-2014

Rishbeth, H. (1971). The *F*-layer dynamo. *Planet. Space Sci.*, *19*(2), 263–267. https://doi.org/10.1016/0032-0633(71)90205-4

Shinbori, A., Sori, T., Otsuka, Y., Nishioka, M., Perwitasari, S., Tsuda, T., Kumamoto, A., Tsuchiya, F., Matsuda, S., … Shinohara, I. (2023). Generation of equatorial plasma bubble after the 2022 Tonga volcanic eruption. *Sci. Rep.*, *13*, 6450. https://doi.org/10.1038/s41598-023-33603-3

Siemes, C., Borries, C., Bruinsma, S., Fernandez-Gomez, I., Hładczuk, N., van den IJssel, J., Kodikara, T., Vielberg, K., and Visser, P. (2023). New thermosphere neutral mass density and crosswind datasets from CHAMP, GRACE, and GRACE-FO. *J. Space Wea. Space Climate*, *13*, 16. https://doi.org/10.1051/swsc/2023014

Song, R., Hattori, K., Zhang, X. M., and Liu, J. Y. (2022). The two-dimensional and three-dimensional structures concerning the traveling ionospheric disturbances over Japan caused by Typhoon Faxai. *J. Geophys. Res.: Space Phys.*, *127*(11), e2022JA030606. https://doi.org/10.1029/2022JA030606

Sori, T., Shinbori, A., Otsuka, Y., Tsugawa, T., and Nishioka, M. (2021). The occurrence feature of plasma bubbles in the equatorial to midlatitude ionosphere during geomagnetic storms using long-term GNSS-TEC data. *J. Geophys. Res.: Space Phys.*, *126*(5), e2020JA029010. https://doi.org/10.1029/2020JA029010

Sun, W. J., Li, G. Z., Zhang, S. R., Hu, L. H., Dai, G. F., Zhao, B. Q., Otsuka, Y., Zhao, X. K., Xie, H. Y., … Perwitasari, S. (2024). Regional ionospheric super bubble induced by significant upward plasma drift during the 1 December 2023 geomagnetic storm. *J. Geophys. Res.: Space Phys.*, *129*(6), e2024JA032430. https://doi.org/10.1029/2024JA032430

Tsunoda, R. T. (1980). Magnetic-field-aligned characteristics of plasma bubbles in the nighttime equatorial ionosphere. *J. Atmos. Terr. Phys.*, *42*(8), 743–752. https://doi.org/10.1016/0021-9169(80)90057-4

Tsunoda, R. T., Livingston, R. C., McClure, J. P., and Hanson, W. B. (1982). Equatorial plasma bubbles: Vertically elongated wedges from the bottomside *F* layer. *J. Geophys. Res.: Space Phys.*, *87*(A11), 9171–9180. https://doi.org/10.1029/ja087ia11p09171

Yang, Z., Morton, Y. T. J., Zakharenkova, I., Cherniak, I., Song, S. L., and Li, W. (2020). Global view of ionospheric disturbance impacts on kinematic GPS positioning solutions during the 2015 St. Patrick's Day storm. *J. Geophys. Res.: Space Phys.*, *125*(7), e2019JA027681. https://doi.org/10.1029/2019JA027681